

Magnetic circular dichroism in hard x-ray Raman scattering as a probe of local spin polarization

Manabu Takahashi

Faculty of Engineering, Gunma University, Kiryu, Gunma 376, Japan

Nozomu Hiraoka

National Synchrotron Radiation Research Center, Hsinchu 30076, Taiwan

Abstract

We argue that the magnetic circular dichroism (MCD) of the hard x-ray Raman scattering (XRS) could be used as an element selective probe of local spin polarization. The magnitude of the XRS-MCD signal is directly proportional to the local spin polarization when the angle between the incident wavevector and the magnetization vector is 135° or -45° . By comparing the experimental observation and the configuration interaction calculation at the $L_{2,3}$ and $M_{2,3}$ edges of ferromagnetic iron, we suggest that the integrated MCD signal in terms of the transferred energy could be used to estimate the local spin moment even in the case where the application of the spin sum-rule in X-ray absorption is questionable. We also point out that XRS-MCD signal could be observed at the M_1 edge with a magnitude comparable to that at the $M_{2,3}$ edge, although the spin-orbit coupling is absent in the core orbital. By combining the XRS-MCD at various edges, spin polarization distribution depending on the orbital magnetic quantum number would be determined.

I. INTRODUCTION

X-ray magnetic circular dichroism (MCD) has been one of the powerful tools to investigate the electronic structure in magnetic materials. Particularly, owing to the orbital and spin sum-rules,^{1,2} the MCD in the soft x-ray absorption spectroscopy (XAS) has been playing crucial roles for elucidating the electronic structure at and around the absorption site.³ The MCD measurements in x-ray emission and resonant inelastic scattering are also important tools to clarify the electronic excitations in magnetic materials.⁴

Recently, the MCD in the hard x-ray Raman scattering (XRS) at the Fe $L_{2,3}$ -edges in the ferromagnetic iron has been investigated.^{5,6} The XRS is a kind of non-resonant inelastic x-ray scattering.⁷ In the process of photon scattering, where an incident photon of energy $\hbar\omega_i$ is absorbed and a photon of energy $\hbar\omega_f$ is emitted, the electron system in the initial ground state of the energy E_i is excited to the final state of the energy $E_f = E_i + \hbar\omega_i - \hbar\omega_f$. The final state of the XRS is essentially the same with that of XAS: A core hole is left behind at the scattering site and an electron is added to the valence or conduction state. Therefore, the XRS intensity as a function of transferred energy is similar to the soft x-ray absorption coefficient as a function of the incident photon energy. Contrasting to the XAS, the hard-in-hard-out feature of the XRS is preferable for bulk sensitive measurements or the measurements under extreme conditions. In addition, the XRS can access the final states that are inaccessible by the dipole transition, because the non-dipole transition matrix elements become significant for shallow core excitation. By virtue of these features, the inner-core-exciting XRS has been demonstrating its usefulness particularly to unveil the electronic state of materials under extreme conditions.⁸ Recently, the electronic state of Fe in Fe_2SiO_4 , Fe_2O_3 and FeS under high pressure is discussed by analyzing the XRS spectra at the Fe $M_{2,3}$ edge, and a spin transition is revealed from the change of spectral curves in FeS.^{9,10} In addition, XRS at the rare earth N and O edges has been extensively discussed.^{11,12}

The XAS-MCD measurements are carried out in order to elucidate the orbital and spin magnetic moment at the selected magnetic ion. In the analysis of the MCD signal, the orbital- and the spin moment sum rules play central roles. However, it is also known that the spin sum rule has some limitations. The core hole level $j = l \pm 1/2$ should be clearly separated for safe application of the sum rule. Teramura et al. showed that the deviation of the rule could amount to 30% for Mn^{2+} and reached at 230% for Sm.^{13,14} The XAS-MCD

signal can be observed also at the $M_{2,3}$ edge of transition metals.^{15,16} However, it is quite difficult to obtain the information about the local spin moment from the observed MCD signal alone, because it is quite hard to apply the spin sum rule due to the smallness of the spin orbit coupling (SOC) of the 3p hole, the strong 3p-3d Coulomb interaction, and the remarkable super-Coster-Kroning decay.¹⁷ The MCD signal at the K-edge of transition metals also have been observed. While it is bulk sensitive, we can only indirectly obtain the information about orbital moment of the 3d state through the interaction between the 3d and 4p states.¹⁸⁻²⁰ It is worth noting that the spin sum rule^{21,22} of the X-ray photoemission spectroscopy, in which both of the photon polarization and the spin of the emitted electron are exploited and the magnetic dichroism is observed in the emission of electrons, can be applied to estimate the ground state spin moment without the aforementioned shortcomings of the XAS-MCD spin sum rule.

The XRS-MCD signals have been observed at the $L_{2,3}$ edges of ferromagnetic iron by Hiraoka et al.⁵ The observe MCD spectral curves as a function of the transferred energy depend strongly on the angle α_M (see fig. 1.), which is similar to the XAS-MCD spectral curve at the angle $\alpha_M \sim 0^\circ$. In the previous paper,⁶ we analyzed the XRS-MCD signals within a one-electron theory and discussed the relation between the spectral shape of the MCD signal and the angle α_M . We elucidated that the XRS-MCD signals can be considered as a result of the interference of the scattering amplitude due to the charge transition with that due to the electric, the orbital magnetic, and the spin magnetic transitions; their effects differently depend on the angle α_M . Particularly, at $\alpha_M = 135^\circ$ or -45° , the magnitude of the XRS-MCD signal is proportional only to the local spin polarization. Therefore, the integrated XRS-MCD signal could be also used as a probe of local spin moment.

The magnetic Compton scattering (MCS) technique,²³ which reveals the distribution of the spin magnetic moment in the momentum space, and the x-ray magnetic diffraction (XMD)²⁴ also owes to the MCD effect. The mechanism causing the MCD in MCS and XMD is different from that in XAS. The interaction between the magnetic field of radiation and the electron spin and/or orbital magnetic moments brings about the MCD effects in MCS and XMD. On the other hand, in the XAS, the spin-orbit coupling in the inner shell plays essential roles in provoking the MCD signal, since the electric field of the radiation does not directly couple to the orbital and spin magnetic moments. In the XRS, both mechanisms can induce the MCD signal with the magnitude comparable to each other. In contrast to the

MCS, XRS-MCD may have advantageous features: the element selectivity and the selection rules in transition process. At $\alpha_M = 135^\circ$, the interference of scattering amplitude due to the charge- and spin-transitions alone produces the MCD signal. Therefore, it is expected that the XRS-MCD measurement could be used as a probe of local spin polarization at the scattering site even if the SOC is absent.

The interaction between the 3p electrons and the 3d electrons is so large that the M-edge excitation spectrum is expected to sensitively reflect the 3d state. Besides the XRS or XAS, the M-edge excitation of transition metal has been well measured using Electron Energy Loss Spectroscopy (EELS), or $K\beta$ x-ray emission spectroscopy (XES). Utilizing the surface sensitivity, the EELS is used to study the electronic structure in thin films.²⁵ The signal of the $K\beta$ XES is bulk sensitive, and the spin dependent spectrum caused by the 3p-3d exchange interaction is useful to elucidate the 3d state.²⁶ The dichroic effect of the Fe $K\alpha_1$ emission spectrum has also recently been observed.²⁷ In addition to these techniques, XRS-MCD may become a useful technique to understand the electronic structures under extreme conditions with exploiting its bulk sensitivity, element and orbital selectivity.

In the next section, we briefly describe the XRS-MCD formula. The model used to simulate the electronic state at the scattering site is described in Section III. In Section IV we discuss the $L_{2,3}$ and $M_{2,3}$ edge XRS spectra by comparing the calculations and the observations. The XRS spectra at the M_1 edge is also demonstrated. The last section is devoted to the concluding remarks. Demonstrations of the XRS-MCD spin sum rule are involved in the last section.

II. SCATTERING INTENSITY AND MCD SIGNAL

We assume that the electronic state is excited from the initial state Φ_i with energy E_i to the final state Φ_f with energy E_f by absorbing an incident photon of polarization \mathbf{e}_i , wave vector \mathbf{q}_i , and energy $\hbar\omega_i$ and emitting a photon of polarization \mathbf{e}_f , wave vector \mathbf{q}_f , and energy of $\hbar\omega_f$. In the final state, a core hole is left behind at the scattering site and an electron is added to the valence or conduction state. The scattering intensity may be proportional to the factor $\sum_{\Phi_f} \left| \langle \Phi_f | \sum_i \hat{f}(\mathbf{x}_i) | \Phi_i \rangle \right|^2 \delta_E$. Here, δ_E represents the energy conservation delta function $\delta(\Delta E + E_i - E_f)$ with $\Delta E = \hbar\omega_i - \hbar\omega_f$; the operator \hat{f} is approximately given by the sum of the charge, electric, orbital magnetic, and spin magnetic transition operators \hat{f}_C ,

\hat{f}_E , \hat{f}_O , and \hat{f}_S , which are given in equations (1a-1d);⁶ \mathbf{x}_i refers to the position \mathbf{r}_i and spin \mathbf{s}_i operators of the i th electron. The transition operators \hat{f}_C , \hat{f}_E , \hat{f}_O , and \hat{f}_S are derived as the first- and second-order perturbation in terms of the interaction between electrons and electromagnetic field in the non-relativistic Hamiltonian.²⁸ The perturbation terms of the higher order than $(\hbar\omega_i/m_e c^2)^2$ may be safely ignored, where $m_e c^2$ is the electron rest energy. To handle the second-order perturbation terms, we assume that a core electron is excited to form an intermediate state Φ_n and the electron successively comes down to an energy level near the lowest unoccupied state to form a final electronic state Φ_f , and take the non-resonant limit, in which we ignore the energy difference between the intermediate electronic state energy E_n and the initial electronic state energy E_i in the energy denominator assuming $E_n - E_i \ll \hbar\omega_i$, $\hbar\omega_f$. Then, we exploit the completeness of the intermediate electronic state Φ_n , and neglect the terms of the order $1 - \omega_f/\omega_i$. Thus, the transition operators may be obtained as

$$\hat{f}_C(\mathbf{x}) = \mathbf{e}_f \cdot \mathbf{e}_i e^{i\mathbf{Q}\cdot\mathbf{r}}, \quad (1a)$$

$$\hat{f}_E(\mathbf{x}) = \frac{i\Delta E}{\alpha m_e c^2} \mathbf{A} \cdot \mathbf{G}(\mathbf{Q}, \mathbf{r}), \quad (1b)$$

$$\hat{f}_O(\mathbf{x}) = -\frac{iE_Q}{2m_e c^2} \mathbf{A} \cdot \hat{\mathbf{Q}} \times \mathbf{L}(\mathbf{Q}, \mathbf{r}), \quad (1c)$$

$$\hat{f}_S(\mathbf{x}) = -\frac{i\bar{E}}{2m_e c^2} \mathbf{h} \cdot \boldsymbol{\sigma} e^{i\mathbf{Q}\cdot\mathbf{r}}, \quad (1d)$$

where $\boldsymbol{\sigma}$, \mathbf{Q} , \mathbf{A} , and \mathbf{h} are defined as $\boldsymbol{\sigma} = 2\mathbf{s}/\hbar$, $\mathbf{Q} = \mathbf{q}_i - \mathbf{q}_f$, $\mathbf{A} = (\mathbf{e}_f \cdot \hat{\mathbf{q}}_i) \mathbf{e}_i + (\mathbf{e}_i \cdot \hat{\mathbf{q}}_f) \mathbf{e}_f$, and $\mathbf{h} = \frac{\hbar\omega_f}{E} (\mathbf{e}_i \cdot \hat{\mathbf{q}}_f) (\hat{\mathbf{q}}_f \times \mathbf{e}_f) - \frac{\hbar\omega_i}{E} (\mathbf{e}_f \cdot \hat{\mathbf{q}}_i) (\hat{\mathbf{q}}_i \times \mathbf{e}_i) + \mathbf{e}_f \times \mathbf{e}_i - (\hat{\mathbf{q}}_f \times \mathbf{e}_f) \times (\hat{\mathbf{q}}_i \times \mathbf{e}_i)$; $\hat{\mathbf{q}}_{i(f)}$ and $\hat{\mathbf{Q}}$ are the unit vectors $\mathbf{q}_{i(f)}/q_{i(f)}$ and \mathbf{Q}/Q , respectively. E_Q , and \bar{E} are energies defined as $E_Q = \hbar c Q$, and $\bar{E} = \hbar(\omega_i + \omega_f)/2$, respectively. α is the fine structure constant. The operators \hat{f}_E and \hat{f}_O are deduced from the terms including the linear momentum operator $\mathbf{p} = -i\hbar\nabla$ using the formula given by Trammel.²⁹ Vectors $\mathbf{G}(\mathbf{Q}, \mathbf{r})$ and $\mathbf{L}(\mathbf{Q}, \mathbf{r})$ are defined as $\mathbf{G}(\mathbf{Q}, \mathbf{r}) = \frac{\alpha^2}{r_e} \mathbf{r} g(\mathbf{Q} \cdot \mathbf{r})$ and $\mathbf{L}(\mathbf{Q}, \mathbf{r}) = \frac{1}{2} \frac{\ell}{\hbar} f(\mathbf{Q} \cdot \mathbf{r}) + f(\mathbf{Q} \cdot \mathbf{r}) \frac{1}{2} \frac{\ell}{\hbar}$ with $g(x) = \frac{1}{ix} (e^{ix} - 1)$, $f(x) = -2i \frac{d}{dx} g(x)$, and $\ell = -i\hbar \mathbf{r} \times \nabla$; r_e is the classical electron radius. We refer to the transition processes described by the operators \hat{f}_C , \hat{f}_E , \hat{f}_O , and \hat{f}_S as C-, E-, O-, and S-transition, respectively.

The XRS-MCD experiment was carried out in the scattering geometry shown in figure 1. The wave vector \mathbf{q}_f is perpendicular to the incident wave vector \mathbf{q}_i . In the experiment, the polarization of the emitted photon is not detected while the incident photon polarization is

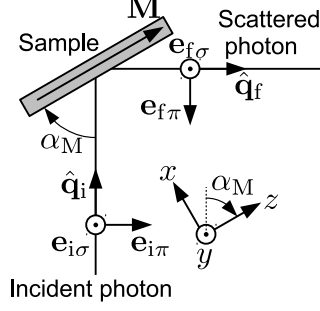


Figure 1. Schematics of scattering geometry in experiment. Coordinate and polarization vectors are defined as shown. α_M is the angle between the magnetization vector \mathbf{M} and the incident propagation vector \mathbf{q}_i . The propagation vectors \mathbf{q}_i and \mathbf{q}_f of incident and emitted x-ray are perpendicular to each other.

controlled. The polarization of the incident photon can be characterized by Stokes parameters P_1 , P_2 , and P_3 .³⁰ Since the magnitude of the C-transition matrix elements are much larger than the others, the total scattering intensity $I_{\text{TOT}} = I(P_1, P_2, P_3) + I(P_1, -P_2, P_3)$ is approximately given only by the C-transition as $(1 + P_3)I_{\text{CC}}^{\sigma\sigma, \sigma\sigma}$ and the MCD signal $I_{\text{MCD}} = I(P_1, |P_2|, P_3) - I(P_1, -|P_2|, P_3)$ is given by $2|P_2| \text{Im}(I_{\text{EC}}^{\sigma\pi, \sigma\sigma} + I_{\text{OC}}^{\sigma\pi, \sigma\sigma} + I_{\text{SC}}^{\sigma\pi, \sigma\sigma})$, where $\text{Im}I$ represents the imaginary part of I ; $I_{\text{EC}}^{\sigma\pi, \sigma\sigma}$ is given by

$$I_{\text{EC}}^{\sigma\pi, \sigma\sigma}(\Delta E) = I_0 \sum_{\Phi_f} \sum_{i, i'} \delta_E \langle \Phi_f | \hat{f}_E^{\sigma\pi}(\mathbf{x}_{i'}) | \Phi_i \rangle^* \langle \Phi_f | \hat{f}_C^{\sigma\sigma}(\mathbf{x}_i) | \Phi_i \rangle, \quad (2)$$

with $I_0 = r_e^2 \omega_f / \omega_i$. Here, the polarization vectors in the transition operator $\hat{f}_E^{\sigma\pi}$ are specified as $\mathbf{e}_f = \mathbf{e}_{f\sigma}$ and $\mathbf{e}_i = \mathbf{e}_{i\pi}$. $I_{\text{CC}}^{\sigma\sigma, \sigma\sigma}$, $I_{\text{OC}}^{\sigma\pi, \sigma\sigma}$, and $I_{\text{SC}}^{\sigma\pi, \sigma\sigma}$ are also given in the same manner.

The XRS intensity may be described as the sum of the scattering intensity from each scattering site. We define the atomic transition matrix elements as

$F_E^{\xi\eta} = \sum_{s_z} \int \psi_\xi^*(\mathbf{r}, s_z) \hat{f}_E^{\sigma\pi}(\mathbf{x}) \psi_\eta(\mathbf{r}, s_z) d\mathbf{r}$, where indices ξ and η refer to one of the spin-orbitals in the 3d states and the 2p or 3p states at the scattering site, respectively; s_z represents the spin magnetic quantum number. $F_C^{\xi\eta}$, $F_O^{\xi\eta}$, and $F_S^{\xi\eta}$ are also defined in the same manner. In the following, the orbital and spin magnetic quantum number of the spin-orbital $\xi(\eta)$ are expressed as $m_{\xi(\eta)}$ and $z_{\xi(\eta)}$. Thus, the wave functions $\psi_\xi(\mathbf{r}, s_z)$ might be given as a product of the radial wave-function $R_\xi(r) = R_{n_\xi l_\xi}(r)$, spherical harmonics $Y_\xi(\hat{\mathbf{r}}) = Y_{l_\xi m_\xi}(\hat{\mathbf{r}})$, and spin function $\chi_\xi(s_z) = \chi_{z_\xi}(s_z)$,³¹ where $n_\xi = 3$, $l_\xi = 2$, $m_\xi = 0, \pm 1, \pm 2$, and $z_\xi = \pm 1/2$. The wave function $\psi_\eta(\mathbf{r}, s_z)$ is also written in the similar form. Functions $e^{i\mathbf{Q}\cdot\mathbf{r}}$, $g(\mathbf{Q}\cdot\mathbf{r})$, and $f(\mathbf{Q}\cdot\mathbf{r})$ can be written in the spherical harmonic expansion

forms $4\pi \sum_{lm} Y_{lm}^* \left(\hat{\mathbf{Q}} \right) i^l w_l(Qr) Y_{lm}(\hat{\mathbf{r}})$, where $w_l(x)$ is $j_l(x)$, $g_l(x)$, and $f_l(x)$; $j_l(x)$ is the spherical Bessel function with degree l , $g_l(x) = \frac{1}{x} \int_0^x j_l(t) dt$ and $f_l(x) = \frac{2}{x^2} \int_0^x t j_l(t) dt$, respectively.

For the scattering geometry as shown in figure 1, the atomic transition matrix elements are written as

$$F_C^{\xi\eta} = 4\pi \sum_{lm} i^l \tilde{j}_l(Q) Y_{lm}^* \left(\hat{\mathbf{Q}} \right) (Y_{lm})_{\xi\eta}, \quad (3a)$$

$$F_E^{\xi\eta} = \frac{4\pi i \Delta E}{\alpha m_e c^2} \sum_{lm\mu} i^l \tilde{g}_l(Q) Y_{lm}^* \left(\hat{\mathbf{Q}} \right) e_{f\sigma}^\mu (\hat{\mathbf{r}}_\mu Y_{lm})_{\xi\eta}, \quad (3b)$$

$$F_O^{\xi\eta} = -\frac{4\pi i E_Q}{m_e c^2} \sum_{lm\mu} i^l \tilde{f}_l(Q) Y_{lm}^* \left(\hat{\mathbf{Q}} \right) \frac{v^\mu ([\ell_\mu Y_{lm}])_{\xi\eta}}{4\hbar}, \quad (3c)$$

$$F_S^{\xi\eta} = \frac{4\pi i \bar{E}}{m_e c^2} \sum_{lm\mu} i^l \tilde{j}_l(Q) Y_{lm}^* \left(\hat{\mathbf{Q}} \right) \hat{q}_f^\mu \left(\frac{\sigma_\mu}{2} Y_{lm} \right)_{\xi\eta}, \quad (3d)$$

where $[\ell_\mu Y_{lm}] = \ell_\mu Y_{lm} + Y_{lm} \ell_\mu$ and the index μ runs over $1, 0, -1$; $\tilde{j}_l(Q)$, $\tilde{g}_l(Q)$, and $\tilde{f}_l(Q)$ are radial integrals $\int R_\xi(r) h(r) R_\eta(r) r^2 d\mathbf{r}$, where $h(r)$ is $j_l(Qr)$, $\frac{\alpha^2}{r_e} r g_l(Qr)$, and $f_l(Qr)$, respectively. The bracket $(A)_{\xi\eta}$ represents the directional integral

$\sum_{s_z} \int Y_\xi^*(\hat{\mathbf{r}}) \chi_\xi(s_z) A(\hat{\mathbf{r}}, \mathbf{s}) Y_\eta(\hat{\mathbf{r}}) \chi_\eta(s_z) d^2\hat{\mathbf{r}}$. The vector components $a^\mu (a_\mu)$ represent the spherical contravariant (covariant) components of vector \mathbf{a} .³¹ \mathbf{v} is given by the vector product $\mathbf{e}_{f\sigma} \times \hat{\mathbf{Q}}$. The contravariant components (a^1, a^0, a^{-1}) of the vectors $\mathbf{e}_{f\sigma}$, $\hat{\mathbf{q}}_f$, \mathbf{v} , and $\hat{\mathbf{Q}}$ can be written, as $(\frac{i}{\sqrt{2}}, 0, \frac{i}{\sqrt{2}})$, $(\frac{C_\alpha}{\sqrt{2}}, S_\alpha, \frac{-C_\alpha}{\sqrt{2}})$, $(-\frac{C_\beta}{\sqrt{2}}, -S_\beta, \frac{C_\beta}{\sqrt{2}})$, and $(-\frac{S_\beta}{\sqrt{2}}, C_\beta, \frac{S_\beta}{\sqrt{2}})$, respectively, where $C_\alpha = \cos \alpha_M$, $S_\alpha = \sin \alpha_M$, $C_\beta = \cos(\alpha_M + \gamma)$, and $S_\beta = \sin(\alpha_M + \gamma)$ with $\gamma \approx \pi/4$.

The angle $\alpha_M = 135^\circ$ is found to be a special angle like as in XMD,³²⁻³⁴ which is called S-position. Because $\mathbf{Q} = (0, -1, 0)$, thereby $Y_{lm}(\hat{\mathbf{Q}}) = \sqrt{(2l+1)/4\pi} \delta_{m0}$, the C-transition conserves both of the total orbital angular momentum L_z and the total spin angular momentum S_z . The E- and O- transition change the orbital angular momentum L_z into $L_z \pm 1$ because the vector components $e_{f\sigma}^0$ and v^0 are zero so that only the matrix elements $(\hat{\mathbf{r}}_{\pm 1} Y_{l0})_{\xi\eta}$ and $([\ell_{\pm 1} Y_{l0}])_{\xi\eta}$ could be non-zero, while they conserve S_z . The S-transition conserves L_z , but changes S_z into any of $S_z \pm 1$ and S_z . Inevitably, if we can assume that the electron system conserves the z component of the total angular momentum $J_z = L_z + S_z$ around the scattering site when the electron system is not affected by the external perturbations, the interference terms $I_{EC}^{\sigma\pi, \sigma\sigma}$ and $I_{OC}^{\sigma\pi, \sigma\sigma}$ would be zero. The terms which involve the spin-off-diagonal S-transition in $I_{SC}^{\sigma\pi, \sigma\sigma}$ also would be zero. Even in case the angular momentum J_z

is not conserved, if the powder approximation are allowed, the effect of such interference terms would not appear on the scattering intensity. Consequently, only the terms which involves the spin-diagonal S-transition in $I_{\text{SC}}^{\sigma\pi,\sigma\sigma}$ can contribute to the XRS intensity as MCD signal. Further, the term $I_{\text{S}\uparrow\text{C}\downarrow}^{\sigma\pi,\sigma\sigma}$ in $I_{\text{SC}}^{\sigma\pi,\sigma\sigma}$ consisting of the S \uparrow -transition, in which an up-spin electron is excited, and the C \downarrow -transition, in which a down electron is excited, and the term $I_{\text{S}\downarrow\text{C}\uparrow}^{\sigma\pi,\sigma\sigma}$ consisting of the S \downarrow -transition and the C \uparrow -transition would not contribute to the XRS intensity, because they have the same magnitude but have the opposite sign to each other. Therefore, putting $M_m = \sum_{\ell} M_m^{(\ell)} = \sum_{\ell} i^{\ell} \sqrt{4\pi(2\ell+1)} \tilde{j}_{\ell}(Q) (Y_{\ell 0})_{2m,1m}$, the term $I_{\text{SC}}^{\sigma\pi,\sigma\sigma}(\Delta E)$ can be simplified as

$$\begin{aligned}
I_{\text{SC}}^{\sigma\pi,\sigma\sigma}(\Delta E) &= \frac{iI_0}{\sqrt{2}} \frac{\bar{E}}{m_e c^2} \sum_{\Phi_f} \delta(\Delta E + E_i - E_f) \\
&\times \sum_{mm'} M_{m'}^* M_m \left\langle \Phi_i \left| p_{m'\uparrow}^{\dagger} d_{m'\uparrow} \right| \Phi_f \right\rangle \left\langle \Phi_f \left| d_{m\uparrow}^{\dagger} p_{m\uparrow} \right| \Phi_i \right\rangle \\
&- \{ \uparrow \longleftrightarrow \downarrow \}.
\end{aligned} \tag{4}$$

If we can assume that the 3p or 2p core states are completely occupied in the initial state Φ_i , the integrated $I_{\text{CC}}^{\sigma\sigma,\sigma\sigma}$ and $I_{\text{SC}}^{\sigma\pi,\sigma\sigma}$ in terms of the transferred energy ΔE can be related to the hole number as

$$\int_{E_E}^{E_C} dx I_{\text{CC}}^{\sigma\sigma,\sigma\sigma}(x) = I_0 N_1, \tag{5a}$$

$$\int_{E_E}^{E_C} dx \text{Im} I_{\text{SC}}^{\sigma\pi,\sigma\sigma}(x) = \frac{I_0}{2\sqrt{2}} \frac{\bar{E}}{m_e c^2} S_1, \tag{5b}$$

where E_E and E_C indicate the transferred energy at the edge and an appropriate cutoff energy, respectively. N_1 and S_1 are defined as $N_1 = \sum_{m=-1}^1 |M_m|^2 (h_{m\uparrow} + h_{m\downarrow})$ and $S_1 = \sum_{m=-1}^1 |M_m|^2 (h_{m\uparrow} - h_{m\downarrow})$, and $h_{m\uparrow(\downarrow)}$ is the up (down) spin hole number in the 3d state specified by the orbital magnetic quantum number m . Thereby, we obtain

$$\frac{S_1}{N_1} = C \frac{\int_{E_E}^{E_C} dx I_{\text{MCD}}(x)}{\int_{E_E}^{E_C} dx I_{\text{TOT}}(x)}, \tag{6}$$

with $C = \sqrt{2} (1 + P_3) m_e c^2 / |P_2| \bar{E}$.

On the other hand, when the angle $\alpha_M = 0$ or 45 degrees, which correspond to the L or L+S position in the XMD, the XRS-MCD signals may show complex behavior because both

of I_{EC} and I_{OC} take part in the MCD signals. For the transition metal M-edge excitation, although the transferred energy ΔE is much smaller than that for the L-edge excitation, the E-transition is not negligible as shown later. If the transferred energy ΔE is so large that the contribution I_{OC} and I_{SC} is negligible, the sum-rules similar to those in the XAS-MCD might be established.

III. MODEL HAMILTONIAN AND CALCULATION METHOD

The configuration interaction (CI) calculation on the Anderson impurity model has been applied to analyze the signals from several core-level spectroscopic experiment on ferromagnetic nickel and have given consistent explanations to the different spectra based on the calculated electronic structure.^{35,36} Although the validity to apply this model for discussion on the spectroscopic properties of more strongly itinerant electron systems is not guaranteed, we exploit the CI calculation on this model as a makeshift to demonstrate the usefulness of the XRS-MCD in this study, because the electron-hole interaction is so large that independent particle approximation may not be suitable for describing the M_{2,3}-edge excitation.

The 3d electron number of the Fe ion could be strongly fluctuating. We assume that the 3d electrons go back and forth between the 3d states under consideration and the electron reservoir states, which are supposed to have d-symmetric states consisting of the 3d and/or 4s states around the scattering site. We prepare the ten different levels $\nu_{\alpha m}$ ($\alpha = 0, 1$ and $m = -2, -1, \dots, 2$) as electron reservoir states. The initial electronic state might be symbolically expressed as $|\Phi_i\rangle = A|d^8\nu^{n_0+2}\rangle + B|d^7\nu^{n_0+3}\rangle + C|d^6\nu^{n_0+4}\rangle$, where $d^m\nu^n$ represents the configuration, in which m electrons occupy the 3d states under consideration and n electrons do the reservoir states. $A|d^m\nu^n\rangle$ represents the linear combination $\sum_c A_c|d^m\nu^n\rangle_c$ over the configurations belonging to the states specified as $d^m\nu^n$.³⁷

We assume the model Hamiltonian for simulating the electronic state as

$$\begin{aligned}
H = & \sum_{\xi} E_d n_{d\xi} + \sum_{\alpha\xi} E_{\alpha} n_{\alpha\xi} + \sum_{\alpha\xi} V \left(d_{\xi}^{\dagger} c_{\alpha\xi} + c_{\alpha\xi}^{\dagger} d_{\xi} \right) \\
& + U_{dd} \sum_{\xi < \xi'} n_{d\xi} n_{d\xi'} + U_{pd} \sum_{\xi\eta} n_{d\xi} n_{p\eta} \\
& + H_{dd} (F_{dd}^2, F_{dd}^4) + H_{pd} (F_{pd}^2, G_{pd}^1, G_{pd}^3) \\
& - \Delta_{\text{mol}} z_{\xi} n_{d\xi} + H_{d\text{SO}} (\zeta_d) + H_{p\text{SO}} (\zeta_p), \tag{7}
\end{aligned}$$

where, d_{ξ}^{\dagger} , d_{ξ} , and $n_{d\xi}$ represent the creation, annihilation, and number operators for the spin-orbital ξ in the 3d state at the site under consideration. $c_{\alpha\xi}^{\dagger}$, $c_{\alpha\xi}$, and $n_{\alpha\xi}$ represent the creation, annihilation, and number operators for the spin orbital $\nu_{\alpha m_{\xi} z_{\xi}}$ in the reservoir states. $n_{p\eta}$ represents the number operator for the spin-orbital η in the 2p or 3p states. The parameters E_d and E_{α} representing the one electron level are assumed to be 0 eV, $-0.2 \times \alpha$ eV. The parameters U_{dd} and U_{pd} corresponding the averaged 3d-3d and 2p(3p)-3d Coulomb interaction are assumed to be 3.5eV and 5.0 (3.5) eV. The hybridization V is assumed to be 1.1 eV. The Slater integrals F_{dd}^2 , F_{dd}^4 , F_{pd}^2 , G_{pd}^1 , and G_{pd}^3 are assumed to be 80% of the atomic values. The parameters ζ_d and ζ_p of the spin-orbit coupling $H_{d\text{SO}}$ and $H_{p\text{SO}}$ are assumed to be the atomic values. These atomic values are calculated by using Cowan code.³⁸ We add the molecular field term $-\Delta_{\text{mol}} z_{\xi} n_{d\xi}$ in order to simulate the ferromagnetic ground state. The parameter Δ_{mol} is assumed to be 1.9eV, which corresponds to the observed exchange splitting value $\varepsilon(\text{H}_{25\uparrow}) - \varepsilon(\text{H}_{25\downarrow})$.³⁹ We numerically diagonalize the Hamiltonian to obtain the initial ground state, in which the d electron number, spin moment, and orbital moment are about 7.0, $2.2\mu_{\text{B}}$, and $0.054\mu_{\text{B}}$, respectively. The weights A , B , and C are $|A|^2 = 23.7\%$, $|B|^2 = 55.7\%$, and $|C|^2 = 20.6\%$, which may be consistent with the stronger itinerancy than ferromagnetic Ni.^{35,36}

Scattering operators $\hat{f}_{\text{E}}^{\sigma\pi}$ can be expressed in the second quantization form using the atomic transition matrix elements $F_{\text{E}}^{\xi\eta}$: $\hat{f}_{\text{E}}^{\sigma\pi} = \sum_{\xi\eta} F_{\text{E}}^{\xi\eta} d_{\xi}^{\dagger} p_{\eta}$ within the model used. The terms $I_{\text{EC}}^{\sigma\pi, \sigma\sigma}$ are given by $I_{\text{EC}}^{\sigma\pi, \sigma\sigma} = \frac{I_0}{2\pi i} \left\langle \Phi_{\text{i}} \left| \hat{f}_{\text{E}}^{\dagger} [R(z) - R(z^*)] \hat{f}_{\text{C}} \right| \Phi_{\text{i}} \right\rangle$, where $R(z) = 1/(z - H)$ with $z = \Delta E + E_{\text{i}} - H - i\Gamma$ and $z^* = \Delta E + E_{\text{i}} - H + i\Gamma$. The other terms $I_{\text{CC}}^{\sigma\sigma, \sigma\sigma}$, $I_{\text{OC}}^{\sigma\pi, \sigma\sigma}$, and $I_{\text{SC}}^{\sigma\pi, \sigma\sigma}$ also can be given in the same manner. To calculate these terms we can use the recursion method with assuming that the final states be described as $|\Phi_{\text{f}}\rangle = A' |p^5 d^9 \nu^{n_0+2}\rangle + B' |p^5 d^8 \nu^{n_0+3}\rangle + C' |p^5 d^7 \nu^{n_0+4}\rangle$, where p^n indicates the states that n electrons are accommodated in the 2p or 3p state. It is well known that the term-dependent

core-hole lifetime due to the 3p-3d3d super-Coster-Kronig decay plays significant roles for explaining the observed spectral shape in the M-edge spectroscopy.⁴⁰ Such core-hole decay processes are not taken into account in our model Hamiltonian. Taguchi et al. assumed that the core-hole lifetime broadening Γ of 3p hole is linear on the relative excitation energy in order to investigate the emission spectra from manganese oxides.²⁶ Although we have no substantial reasons, we assume the broadening Γ linearly depending on the relative excitation energy, when comparing the calculated and observed spectra at the $M_{2,3}$ edge.

As shown later, we obtain plausible results for both of the $L_{2,3}$ and $M_{2,3}$ edges XRS spectra. The spectral shape is not sensitive on the model parameters as far as we use the initial state in which the 3d electron number is about 7.0 and the spin moment is about $2.2\mu_B$. However, the validity of the calculated spectra based on the above mentioned approximation is probably quite limited. In the spectral shape at the $M_{2,3}$ edge, several inconsistencies are found between the observation and the calculation. Nevertheless, we hope that the results are of value to provide insight into the XRS-MCD and understand its usefulness.

IV. RESULTS AND DISCUSSIONS

A. Fe $L_{2,3}$ edge

In the previous papers,^{5,6} we investigated the XRS-MCD at the Fe $L_{2,3}$ edge within independent particle approximation using band structure calculation based on the local spin density approximation. At the $L_{2,3}$ edge, the dipole transitions dominates the scattering intensity and the MCD signal, in which the form factors $\tilde{j}_1(Q)$, $\tilde{g}_0(Q)$, and $\tilde{f}_1(Q)$ are relevant. In figure 2, we compare the total intensities calculated by the CI calculation and the band calculation with the experimental observation.⁴¹ Both of the calculations well reproduce the observed spectral curve. The observed L_3 peak, concentrating around the transferred energy 705 ~ 714eV, looks consisting of a main peak about 708eV and a shoulder structure around 712eV. This shoulder structure seems not to be properly reproduced by the calculations: The one-body calculation does not give the shoulder structure, on the other hand the CI calculation seems to provide too strong intensity for the shoulder structure.

The total intensity after background subtraction and the MCD signals are shown in figure 3 in comparison with those obtained by the CI calculation. The Stokes parameters of the

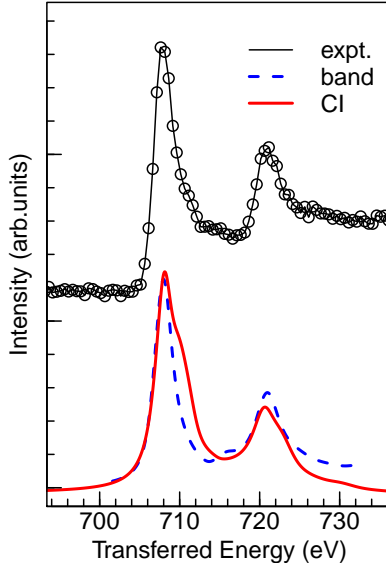


Figure 2. (color on line) Total XRS intensity as a function of the transferred energy and the calculated intensity I_{CC} . Thin solid line with circle symbol represents the observed intensity without background subtraction. Thick solid, and broken lines are the spectral curves calculated by the CI calculation and the band structure calculation, respectively. Lifetime broadening is assumed to be $\Gamma_3 = 1.4$ and $\Gamma_2 = 0.9$ eV.

incident beam polarization are assumed as $|P_2| = 0.6$ and $P_3 = -0.8$. The CI calculation well reproduces the observed MCD signals both on the relative intensity to the total intensity, the sign of MCD signal, and their dependence on the angle α_M . In the most right panels, the spectral curves of the intensity I_{CC} , and the MCD components $\text{Im}I_{EC}$, $\text{Im}I_{OC}$, and $\text{Im}I_{SC}$ at the angle $\alpha_M = 0^\circ$ and 135° are also shown. At the angle $\alpha_M = 0^\circ$, $\text{Im}I_{EC}$ dominantly contributes to the total MCD signal, while at the angle $\alpha_M = 135^\circ$, $\text{Im}I_{EC}$ and $\text{Im}I_{OC}$ are completely suppressed and only $\text{Im}I_{SC}$ contributes to the total MCD signal. We note that at the angle $\alpha_M = 0^\circ$, the MCD component $\text{Im}I_{SC}$ is not completely zero; it would be zero if we assume the powder approximation. The results obtained by the CI calculation are essentially the same with those calculated by the band calculation⁶.

B. Fe $M_{2,3}$ edge

The relative magnitude of $\text{Im}I_{SC}$ to I_{CC} is independent of the edges, because I_{SC} is directly proportional to the 3d spin moment in accordance with eq. (4). At the Fe $M_{2,3}$

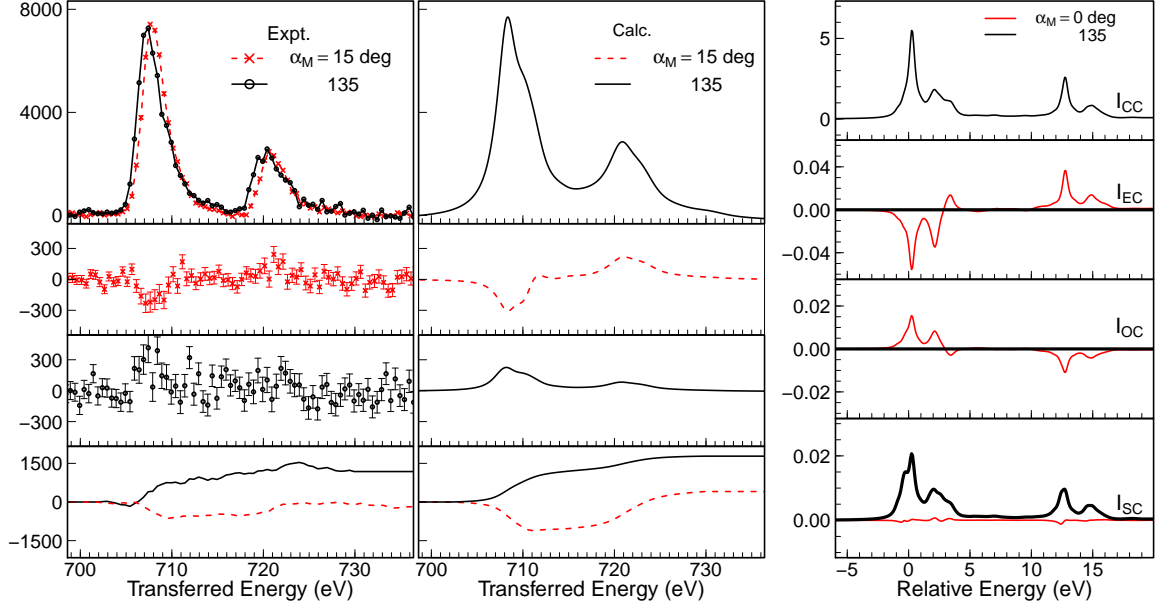


Figure 3. (color online) The observed total intensity after background subtraction (left) and the calculated total intensity (center) are shown in the top panels, respectively. The total XRS signals at $\alpha_M = 15^\circ$ and 135° are shown with red dashed and black solid curves. MCD signals at the corresponding angle α_M are shown in the second and third rows. The integrated MCD signals are shown in bottom panels. In the right panels, the spectral curves of the intensity I_{CC} , $\text{Im}I_{EC}$, $\text{Im}I_{OC}$, and $\text{Im}I_{SC}$ at the angles $\alpha_M = 0^\circ$ and 135° are shown with lifetime broadening $\Gamma = 0.14\text{eV}$.

edge, the MCD signal at the angle $\alpha_M = 135^\circ$ might be observed with the same relative magnitude to the total intensity as at the $L_{2,3}$ edge. At the Fe $M_{2,3}$ edge the octupole transition becomes significant as well as the dipole transition for the high Q scattering. Figure 4 shows the observed and calculated total intensities as a function of the transferred energy at the scattering angles $2\theta = 23^\circ$ and 90° , which correspond to the scattering vector $Q = 1.1$ and 3.5 a.u., respectively. At the scattering angle $2\theta = 23^\circ$, the intensity is dominated by the dipole transition. As the scattering vector becomes larger, the octupole transition become dominant and the dipole transition becomes subordinate; the intensity around the transferred energy $53 \sim 55$ eV become intense and the intensity above 55 eV becomes weak. A similar tendency can be seen in the XRS spectra on iron oxides.¹⁰ In order to compare the observation and the calculation, we naively assume that the lifetime broadening is $\Gamma = \max(0.1E + 0.14, 0.14)$ eV, where E is the relative transferred

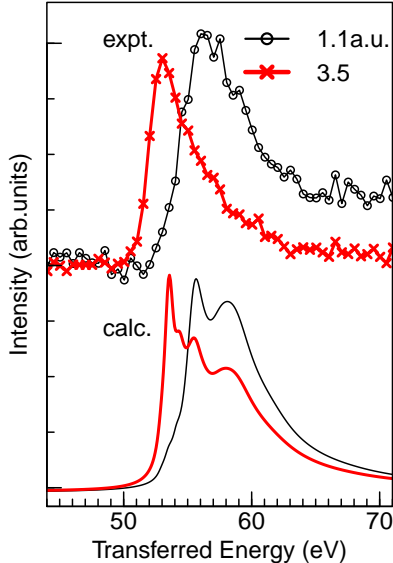


Figure 4. (Color online) Observed and calculated total XRS intensities as a function of the transferred energy. Black thin and red thick lines are the intensities at the scattering vector $Q = 1.1$ and 3.5 a.u. corresponding to the scattering angles $2\theta = 23^\circ$ and 90° , respectively.

energy from the edge. Although the calculated spectra resemble the observed one, they show discernible inconsistencies at the scattering angle $2\theta = 90^\circ$. In comparison with the observed spectra, the calculated intensity above the transferred energy 55 eV, which is mainly caused by the dipole transition, looks to be quite overestimated, or the intensity around the transferred energy 53 eV, which is mainly caused by the octupole transition, looks to be underestimated. In order to improve the calculated spectral curve, it might be necessary to explicitly take account of the super-Coster-Kroning decay process into the calculation. In the vicinity of the edge, the low-lying electron-hole-pair excitations might be essential for the shape of the peak.^{42,43} In spite of the noticeable deviation between the experimental observation and the calculation, we expect that the results could give us better understanding of the XRS-MCD.

Left panel in figure 5 shows the observed spectra as a function of the transferred energy at the angles $\alpha_M = 15^\circ$ and 135° . Contrasting to the L-edge spectra, the spectral curve of the MCD signal at $\alpha_M = 15^\circ$ is rather simple: its magnitude is very weak and the shape is similar to that at $\alpha_M = 135^\circ$, which are also similar to the total intensity. This might suggest that the contribution of $\text{Im}I_{\text{EC}}$ and $\text{Im}I_{\text{OC}}$ are suppressed and $\text{Im}I_{\text{SC}}$ dominates the MCD signal. Right panel shows the calculated spectra corresponding to the observation

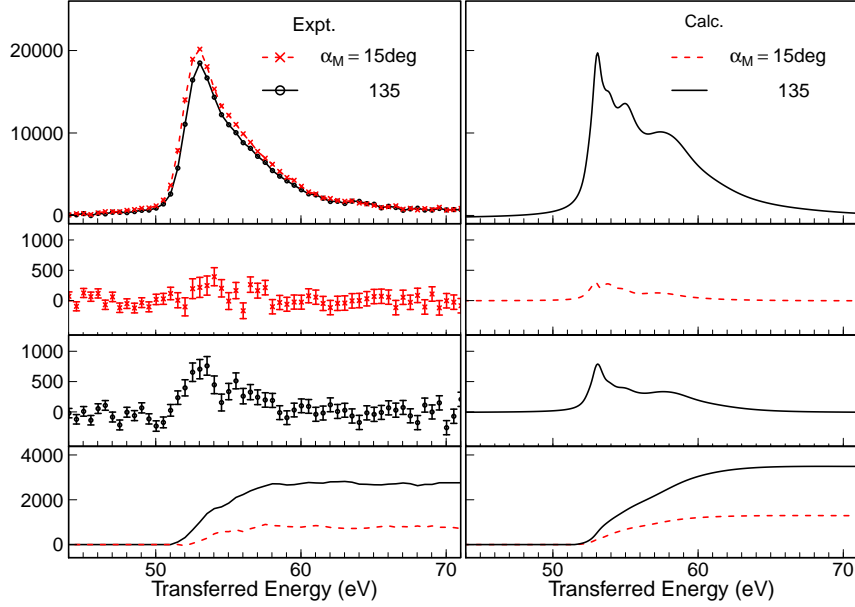


Figure 5. (color online) Observed spectra (left panel) and calculated spectra (right panel) are shown as a function of the transferred energy. The total intensity after subtracting the background, the MCD signal, and the integrated MCD signal are shown in top, middle, and bottom panels. The signals for the angle $\alpha_M = 15^\circ$ and 135° are indicated by red cross symbols and broken lines, and the black circle symbols and solid lines.

with the polarization parameters $|P_2| = 0.6$ and $P_3 = -0.8$. The sign of the MCD signal, the relative magnitude of the MCD signal to the total intensity and the shape of the spectral curves are rather well reproduced by the calculation.

The left panel in figure 6 shows the intensities I_{CC} , $\text{Im}I_{EC}$, $\text{Im}I_{OC}$, and $\text{Im}I_{SC}$ as a function of the relative energy of the final states at the angle $\alpha_M = 0^\circ$, 15° , and 135° . It is found that $\text{Im}I_{EC}$ and $\text{Im}I_{OC}$ can be almost canceled out to each other near $\alpha_M = 0^\circ$. Consequently, the MCD signal at $\alpha_M = 15^\circ$ are dominated by $\text{Im}I_{SC}$. At the L-edge, this cancellation is insufficient: $\text{Im}I_{EC}$ dominates the MCD signals at $\alpha_M = 15^\circ$. At $\alpha_M = 135^\circ$, the MCD signals due to $\text{Im}I_{EC}$ and $\text{Im}I_{OC}$ are completely suppressed, so $\text{Im}I_{SC}$ alone contributes to the MCD signals. Thus, the MCD signals reflect only the spin polarization in the 3d orbitals of the orbital magnetic quantum number $m = 0, \pm 1$. It may be worth noting again that $\text{Im}I_{SC}$ is not identically zero even at the angle $\alpha_M = 0^\circ$.

The left panel in figure 6 shows the calculated intensities due to the dipole transition alone and the octupole transition alone. The dipole and octupole transitions dominate the

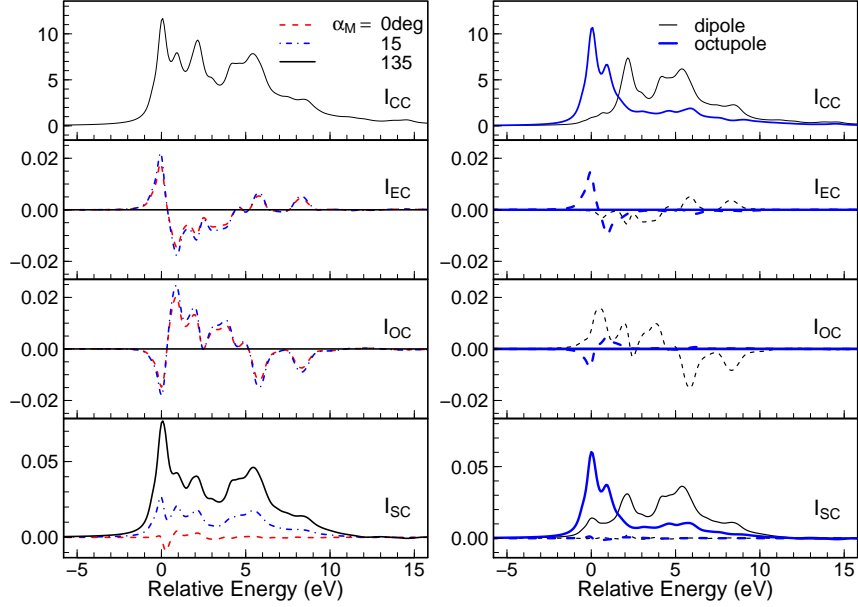


Figure 6. (Color online) Left panels show the intensities I_{CC} , $\text{Im}I_{EC}$, $\text{Im}I_{OC}$, and $\text{Im}I_{SC}$ from top to bottom as a function of relative energy of the final states at $\alpha_M = 0$ (dashed line), 15° (dot-dash line) and 135° (solid line). Right panels show the decomposed intensities into the parts due to the dipole (thin line) and octupole (thick line) transition processes. Dashed and solid curves indicate the results at the angle $\alpha_M = 0^\circ$ and 135° . The life time broadening is assumed to be $\Gamma = 0.14$ eV.

intensities in the range of $2.5 \sim 10$ eV and the range of $0 \sim 2.5$ eV, respectively. The effect of the interference between them does not look significant in the intensity I_{CC} . On the other hand it could not be ignored for producing the spectral structure of the MCD signal. Therefore, the detailed information about the electronic structure might be obtained from the analysis of the XRS-MCD signal.

C. M_1 edge

The MCD signal would be observed even at the M_1 edge with the magnitude comparable to the $M_{2,3}$ edge, because I_{SC} reflects the 3d spin polarization through the interaction $\mathbf{h} \cdot \boldsymbol{\sigma}$ between the electron spin and the radiation field in Eq. (1d). The quadrupole transition, in which the factors $\tilde{j}_2(Q)$, $\tilde{g}_1(Q)$, and $\tilde{f}_2(Q)$ are relevant, dominates the excitation process ($3s \rightarrow 3d$) at the M_1 edge. Due to the absence of the SOC in the 3s orbital, $\text{Im}I_{EC}$ and $\text{Im}I_{OC}$ are supposed to be small; those signals just reflect the 3d orbital polarization due to the

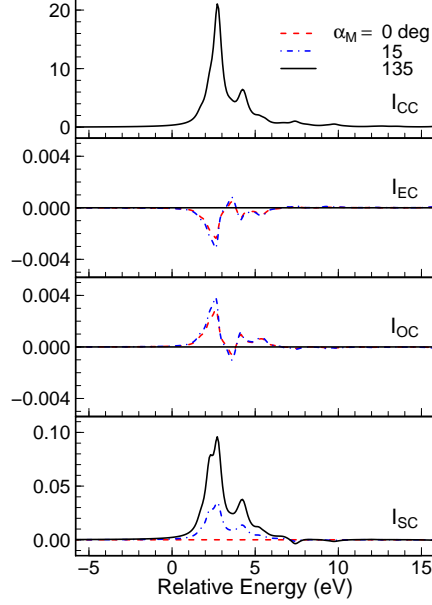


Figure 7. (Color online) The intensity I_{CC} and the MCD components $\text{Im}I_{EC}$, $\text{Im}I_{OC}$, and $\text{Im}I_{SC}$ as a function of relative energy of the final states at $\alpha_M = 0^\circ$ (dashed line), 15° (dot-dash line) and 135° (solid line) for the M_1 edge XRS. The life time broadening is assumed to be $\Gamma = 0.14$ eV.

SOC in the 3d states. It is expected that $\text{Im}I_{SC}$ would be as large as that in the $M_{2,3}$ edge. Thus, the MCD signal caused by only the 3d spin polarization would be observed.

In figure 7, the calculated M_1 edge XRS and the MCD spectra are shown. The relative magnitude of the MCD signal to the total intensity is in the same order with that in the $M_{2,3}$ edge spectra at the angle $\alpha_M = 135^\circ$. At this angle α_M , the MCD components $\text{Im}I_{EC}$ and $\text{Im}I_{OC}$ are suppressed, so that the component $\text{Im}I_{SC}$ alone contributes to the MCD signal. Therefore, the MCD signal reflects only the spin moment of the 3d orbital with the orbital magnetic quantum number $m = 0$. At the angle $\alpha_M = 0^\circ$, the component $\text{Im}I_{SC}$ is almost suppressed because the SOC in 3s orbital is absent and the SOC in the 3d orbital is very small. The components $\text{Im}I_{EC}$ and $\text{Im}I_{OC}$ only weakly contribute to the MCD signal due to the smallness of the SOC in 3d orbital. Because they are very small and have opposite sign to each other, the total MCD signal would be too small to be observed at the present stage.

Putting $M'_0 = -\sqrt{12\pi}\tilde{j}_2(Q)(Y_{20})_{20,00}$, the integrated intensity $I_{CC}^{\sigma\sigma,\sigma\sigma}$ and component $\text{Im}I_{SC}^{\sigma\pi,\sigma\sigma}$ at the angle $\alpha_M = 135^\circ$ might be given by

$\int_{E_E}^{E_C} dx I_{CC}^{\sigma\sigma,\sigma\sigma}(x) = I_0 M_0'^2 (h_{0\uparrow} + h_{0\downarrow})$, and $\int_{E_E}^{E_C} dx \text{Im}I_{SC}^{\sigma\pi,\sigma\sigma}(x) = \frac{1}{2\sqrt{2}} \frac{\tilde{E}}{m_e c^2} I_0 M_0'^2 (h_{0\uparrow} - h_{0\downarrow})$, respectively. Therefore, the ratio of the integrated MCD signals to the integrated in-

tensity could give the spin polarization ratio $(h_{0\uparrow} - h_{0\downarrow}) / (h_{0\uparrow} + h_{0\downarrow})$ in the 3d orbitals with the magnetic quantum number $m = 0$ as $C \int_{E_E}^{E_C} dx I_{\text{MCD}}(x) / \int_{E_E}^{E_C} dx I_{\text{TOT}}(x)$ with $C = \sqrt{2}(1 + P_3) m_e c^2 / |P_2| \bar{E}$.

V. CONCLUDING REMARKS

We investigated the XRS-MCD spectra by comparing the observed and the theoretically calculated spectra at the $L_{2,3}$ and $M_{2,3}$ edges of ferromagnetic iron. We used the configuration interaction calculation on the Anderson impurity model as a makeshift to simulate the electronic structure of iron at the scattering center. The calculation reproduced the observed spectra rather well in spite of the awkward approximation for the strongly itinerant system. For more detailed analysis, we would need a more sophisticated approximation and a model which could appropriately reproduce the multiplet structure in the excited state with taking into account both of the localized and itinerant nature of the 3d electrons in the ferromagnetic iron. For the localized electronic systems, the model used here may give more plausible results.

The MCD signals consist of the three components $\text{Im}I_{\text{EC}}$, $\text{Im}I_{\text{OC}}$, and $\text{Im}I_{\text{SC}}$. Their angle α_M dependences of them are different. Particularly, at $\alpha_M = 135^\circ$ in the right angle scattering condition, $\text{Im}I_{\text{EC}}$ and $\text{Im}I_{\text{OC}}$ are suppressed if the total J_z around the scattering site is conserved or in the situation where the powder approximation is proper. At this scattering geometry, the orbital magnetic quantum number m is conserved both in the C- and S- transitions. The intensity I_{CC} is proportional to the 3d hole number, while the MCD component $\text{Im}I_{\text{SC}}$ is proportional to the difference of the number of the up and down 3d holes. Therefore, the information of the spin polarization in the 3d orbitals with the magnetic quantum numbers $m = 0, \pm 1$ may be obtained.

Here, we demonstrate the XRS-MCD spin sum rule at $\alpha_M = 135^\circ$. The ratios of the integrated MCD signal and the total signal in the observation $\int_{E_E}^{E_C} I_{\text{MCD}}(x) dx / \int_{E_E}^{E_C} I_{\text{TOT}}(x) dx$ is estimated to be $0.025 \sim 0.031$ at the $L_{2,3}$ edge with $E_E = 700 \sim 705$ and $E_C = 730 \sim 740$ eV. The ratio at the $M_{2,3}$ edge is estimated to be $0.024 \sim 0.029$ with $E_E = 45 \sim 51$ and $E_C = 70 \sim 80$ eV. Using Eq. (6), these ratios lead to the spin polarization ratio S_1/N_1 as $0.59 \sim 0.73$ for the $L_{2,3}$ -edge assuming $\bar{E} = 10.2$ keV and $0.58 \sim 0.70$ for the $M_{2,3}$ -edge assuming $\bar{E} = 9.9$ keV. The value S_1/N_1 obtained by the CI calculation is 0.744 for both

the $L_{2,3}$ - and $M_{2,3}$ -edges. Assuming that the 3d states accommodate 3.0 holes per an iron atom, that $h_{0\uparrow(\downarrow)}$, $(h_{1\uparrow(\downarrow)} + h_{1\downarrow(\downarrow)})/2$, and $(h_{2\uparrow(\downarrow)} + h_{2\downarrow(\downarrow)})/2$ equal to each other, the local spin moment is estimated to be $1.7 \sim 2.3\mu_B$. The estimated value of the spin moment has large ambiguity at present mainly due to smallness of the signal accumulation, we hope that the difficulties in XRS-MCD experiment will be over in future with the progress of the instrumentation.

We also demonstrated the XRS-MCD at the M_1 edge. Because the MCD components $\text{Im}I_{\text{EC}}$ and $\text{Im}I_{\text{OC}}$ are mainly caused by the SOC in the core state, they are almost suppressed and only weakly induced by the SOC in the 3d state. On the other hand, the magnitude of the MCD component $\text{Im}I_{\text{SC}}$ is comparable to that for $M_{2,3}$ edge because it reflects the spin polarization in the 3d state. At the angle $\alpha_M = 135^\circ$, it reflects the spin polarization in the 3d state with the magnetic quantum number $m = 0$. Therefore, the information of the spin polarization in the 3d orbitals with the magnetic quantum numbers $m = 0$ can be obtained. By analyzing the MCD spectra at the M_1 -edge together with the $M_{2,3}$ edge, it might be possible to obtain the orbital resolved spin polarization. We have not yet known such a simple procedure to obtain the information on the orbital moment so far.

It is well known that the application of the spin sum rule in the XAS-MCD requires careful consideration.^{13,14} Contrasting to the XAS-MCD, the sum rules (5a) and (5b) do not subject to such a restriction. At angle $\alpha_M = 135^\circ$, the transition processes leading to the MCD component $\text{Im}I_{\text{SC}}$ and the intensity I_{CC} are almost equivalent. Every final state due to the C-transition and the S-transition coincide. In the S-transition, the sign of the scattering amplitude is determined by the spin magnetic quantum number of the excited electron. Thus, it is expected that any decay processes result in the same effect on the spectral shape of the total XRS intensity and the MCD signal. Therefore, analyzing the total intensity and the MCD signal, we would be able to obtain the information of the spin polarization in the 3d state. If we exploit the M_1 , $M_{2,3}$, and $M_{4,5}$ excitations to investigate the 4d states, the orbital decomposed ($|m| = 0, 1, 2$) information about the spin polarization could be obtained. At angle $\alpha_M = 135^\circ$, the total intensity and the MCD signal would show a quite similar spectral curves to each other for the complete ferromagnetic state. For the incomplete ferromagnetic state, these might show different spectral curves. The spin resolved spectral curves might be obtained by analyzing the total intensity and the MCD signal. We hope the XRS-MCD will become one of useful tools to investigate the spin polarization of

the magnetic ions such as the XMD and the MCS.

Acknowledgment

Author M.T. thanks Arata Tanaka for his kindness to allow us to use the Xtls code adapted to our calculation and fruitful discussions. The experiment was performed at BL12XU/SPring-8 with approvals of SPring-8 and National Synchrotron Radiation Research Center, Taiwan (Proposal No. 2016B4252/2016-2-042).

-
- ¹ P. Carra, B. T. Thole, M. Altarelli, and X. Wang, *Physical Review Letters* **70**, 694 (1993).
 - ² B. T. Thole, P. Carra, F. Sette, and G. van der Laan, *Physical Review Letters* **68**, 1943 (1992).
 - ³ T. Nakamura and M. Suzuki, *Journal of the Physical Society of Japan* **82**, 021006 (2013).
 - ⁴ A. Kotani and S. Shin, *Reviews of Modern Physics* **73**, 203 (2001).
 - ⁵ N. Hiraoka, M. Takahashi, W. B. Wu, C. H. Lai, K. D. Tsuei, and D. J. Huang, *Physical Review B* **91**, 241112(R) (2015).
 - ⁶ M. Takahashi and N. Hiraoka, *Physical Review B* **92**, 094441 (2015).
 - ⁷ J.-P. Rueff and A. Shukla, *Reviews of Modern Physics* **82**, 847 (2010).
 - ⁸ C. Sternemann and M. Wilke, *High Pressure Research* **36**, 275 (2016).
 - ⁹ A. Nyrow, C. Sternemann, M. Wilke, R. A. Gordon, K. Mende, H. Yavaş, L. Simonelli, N. Hiraoka, C. J. Sahle, S. Huotari, G. B. Andreozzi, A. B. Woodland, M. Tolan, and J. S. Tse, *Contributions to Mineralogy and Petrology* **167**, 1012 (2014).
 - ¹⁰ A. Nyrow, J. S. Tse, N. Hiraoka, S. Desgreniers, T. Buning, K. Mende, M. Tolan, M. Wilke, and C. Sternemann, *Applied Physics Letters* **104**, 262408 (2014).
 - ¹¹ G. van der Laan, *Physical Review B* **86**, 035138 (2012).
 - ¹² S. Huotari, E. Suljoti, C. J. Sahle, S. Radel, G. Monaco, and F. M. F. de Groot, *New Journal of Physics* **17**, 043041 (2015).
 - ¹³ Y. Teramura, A. Tanaka, and T. Jo, *Journal of the Physical Society of Japan* **65**, 1053 (1996).
 - ¹⁴ Y. Teramura, A. Tanaka, B. T. Thole, and T. Jo, *Journal of the Physical Society of Japan* **65**, 3056 (1996).
 - ¹⁵ A. Yoshida and T. Jo, *Journal of the Physical Society of Japan* **60**, 2098 (1991).

- ¹⁶ T. Koide, T. Shidara, H. Fukutani, K. Yamaguchi, A. Fujimori, and S. Kimura, *Physical Review B* **44**, 4697 (1991).
- ¹⁷ D. Coster and R. D. L. Kronig, *Physica* **2**, 13 (1935).
- ¹⁸ J. Igarashi and K. Hirai, *Physical Review B* **50**, 17820 (1994).
- ¹⁹ J. Igarashi and K. Hirai, *Physical Review B* **53**, 6442 (1996).
- ²⁰ C. Brouder, M. Alouani, and K. H. Bennemann, *Physical Review B* **54**, 7334 (1996).
- ²¹ B. T. Thole and G. van der Laan, *Physical Review Letters* **70**, 2499 (1993).
- ²² G. van der Laan and B. T. Thole, *Physical Review B* **48**, 210 (1993).
- ²³ M. Cooper, P. Mijnarends, N. Shiotani, N. Sakai, and A. Bansil, *X-Ray Compton Scattering* (Oxford University Press, New York, 2004).
- ²⁴ M. Blume, *Journal of Applied Physics* **57**, 3615 (1985).
- ²⁵ L. A. Garvie and P. R. Buseck, *American Mineralogist* **89**, 485 (2004).
- ²⁶ M. Taguchi, T. Uozumi, and A. Kotani, *Journal of the Physical Society of Japan* **66**, 247 (1997).
- ²⁷ T. Inami, *Physical Review Letter* **119**, 137203 (2017).
- ²⁸ J. Fröhlich and U. M. Studer, *Reviews of Modern Physics* **65**, 733 (1993).
- ²⁹ G. T. Trammell, *Physical Review* **92**, 1387 (1953).
- ³⁰ V. B. Berestetskii, E. M. Lifshitz, and L. P. Pitaevskii, *Quantum Electrodynamics* (Elsevier, New York, 1982) p. ii.
- ³¹ D. A. Varshalovich, A. N. Moskalev, and V. K. Khersonskii, *Quantum Theory of Angular Momentum* (World Scientific, Singapore, 1988).
- ³² M. Blume and D. Gibbs, *Physical Review B* **37**, 1779 (1988).
- ³³ S. W. Lovesey, *Journal of Physics C: Solid State Physics* **20**, 5625 (1987).
- ³⁴ D. Laundry, S. P. Collins, and A. J. Rollason, *Journal of Physics: Condensed Matter* **3**, 369 (1991).
- ³⁵ T. Jo and G. A. Sawatzky, *Physical Review B* **43**, 8771 (1991).
- ³⁶ A. Tanaka, T. Jo, and G. A. Sawatzky, *Journal of the Physical Society of Japan* **61**, 2636 (1992).
- ³⁷ We assumed $n_0 = 4$, which gives most plausible results.
- ³⁸ R. Cowan, *The Theory of Atomic Structure and Spectra*, Los Alamos Series in Basic and Applied Sciences (University of California Press, Berkeley, 1981).
- ³⁹ A. Santoni and F. J. Himpsel, *Physical Review B* **43**, 1305 (1991).

- ⁴⁰ K. Okada, A. Kotani, H. Ogasawara, Y. Seino, and B. T. Thole, *Physical Review B* **47**, 6203 (1993).
- ⁴¹ In the experiments at the L- and M-edges, the incident photon energy is scanned over a specific range to detect emitted photons with an energy of 9888 eV.
- ⁴² S. Doniach, P. M. Platzman, and J. T. Yue, *Physical Review B* **4**, 3345 (1971).
- ⁴³ P. Nozières and E. Abrahams, *Physical Review B* **10**, 3099 (1974).